Dual-Band Wireless Power Transfer With Reactance Steering Network and Reconfigurable Receivers

Ming Liu, *Member, IEEE*, and Minjie Chen, *Member, IEEE*

***Abstract*—Wireless power transfer (WPT) via near-field magnetic coupling is an enabling technology for many applications. A few WPT standards are under development with frequencies ranging from kilohertz (kHz) to megahertz (MHz). Operation in kHz offers a higher power rating and that in MHz offers a smaller size. This paper presents a dual-band WPT architecture with novel transmitter and receiver topologies that can achieve high performance at both 100 kHz and 13.56 MHz with low component count and decoupled power delivery at different frequencies. On the transmitter side, we introduce an enhanced push–pull Class-E topology together with a reactance steering network (RSN), which can seamlessly compensate the load impedance variation for MHz wireless power transmitters. On the receiver side, we present a reconfigurable dual-band rectifier that can achieve a power density of 300 W/in^3 with low component count and low total harmonic distortion. A complete dual-band WPT system comprising an RSN-based dual-band transmitter and multiple reconfigurable receivers has been built and tested. The WPT system can simultaneously deliver a total of 30 W of power to multiple receivers (15 W maximum each) with 82.5% efficiency at 100 kHz and 74.8% efficiency at 13.56 MHz with 2.8 cm of coil distance and up to 5 cm of coil misalignment.**

***Index Terms*—Dual-band wireless power transfer (WPT), high-frequency (HF) power conversion, radio frequency power amplifiers, reactance steering network (RSN), reconfigurable rectifier.**

I. Introduction

WIRELESS power transfer (WPT) through near-field magnetic coupling is an enabling technology for many applications including consumer electronics and industrial applications [1]–[5]. A few WPT standards have been established (e.g., AirFuel, Qi) with frequencies ranging from hundreds of kilohertz (kHz) to a few megahertz (MHz). These standards may merge and may cover many frequency domains in the future. In general, there is a fundamental tradeoff between kHz operation and MHz operation in WPT: MHz operation enables long distance power transfer and better robustness against coil misalignment, whereas kHz operation offers higher efficiency and higher power transfer capability [6]. Both kHz and MHz WPT systems may co-exist for a long period of time. Many WPT equipped devices may co-locate in the same electromagnetic domain in many application scenarios (e.g., wireless powered desktop, wireless powered working bench). Emerging designs also need to be back-compatible with previous standards and need to be software upgradable (e.g., WPT in vehicles and robotics). High-performance multi-band transmitters that can power multiple receivers at different frequencies and miniaturized multi-band receivers that can receive power from a variety of transmitters are needed and are the main focus of this paper.

Many dual-band WPT systems have been developed [7]–[12]. Full-bridge inverter topologies are highly preferable in the kHz range, and single switch Class-E derived topologies are widely used in the MHz range. These existing solutions usually focus on the design of the passive network and the coils. This paper aims to push the performance boundary of dual-band WPT with better transmitter and receiver architectures. In the MHz range, maintaining resistive load is critical (e.g., for Class-E converters [13]). There exist many design techniques that can compress the load resistance variation [14]–[21]. However, for reactance variation, the most commonly adopted solution is to use a separate tunable matching network [22]. Sinha *et al.* [23] present a variable reactance rectifier, which helps to address the challenge from the receiver side. However, the additional passive components and switching devices increase the component count and the volume. On the receiver side, full-bridge rectifiers can offer high efficiency and high tolerance to impedance variation for 100-kHz operation. For MHz operation, Class-E-based rectifiers are very promising as they offer high performance with low component count and low total harmonic distortion (THD). Since receivers are usually co-packaged with portable devices or electric vehicles with size and thermal limits, low component count and small size are attractive [24].

This paper presents a few novel WPT topologies and architectures on both the transmitter side and the receiver side to achieve high efficiency with wide impedance variation range and low component count. Advantages are created by adopting the multi-track and partial power processing concepts [25]–[28]. On the transmitter side, we introduce a reactance steering network (RSN) enabled dual-band transmitter [29], which can independently modulate the power delivered at two frequencies. On the receiver side, we present a reconfigurable dual-band receiver that can maintain high performance at both frequencies with low switch count and high power density. The dual-band receiver

Manuscript received December 11, 2018; revised March 15, 2019; accepted April 22, 2019. Date of publication April 28, 2019; date of current version October 18, 2019. This work was supported in part by the National Science Foundation under Award #1847365, in part by the Andlinger Center for Energy and the Environment, Princeton University, and in part by the Siebel Energy Institute. Recommended for publication by Associate Editor H. Hofmann. *(Corresponding author: Minjie Chen.)*

The authors are with the Department of Electrical Engineering and the Andlinger Center for Energy and the Environment, Princeton University, Princeton, NJ 08540 USA (e-mail: ml45@princeton.edu; minjie@princeton.edu).

Color versions of one or more of the figures in this paper are available online at http://ieeexplore.ieee.org.

Digital Object Identifier 10.1109/TPEL.2019.2913991

See http://www.ieee.org/publications_standards/publications/rights/index.html for more information.

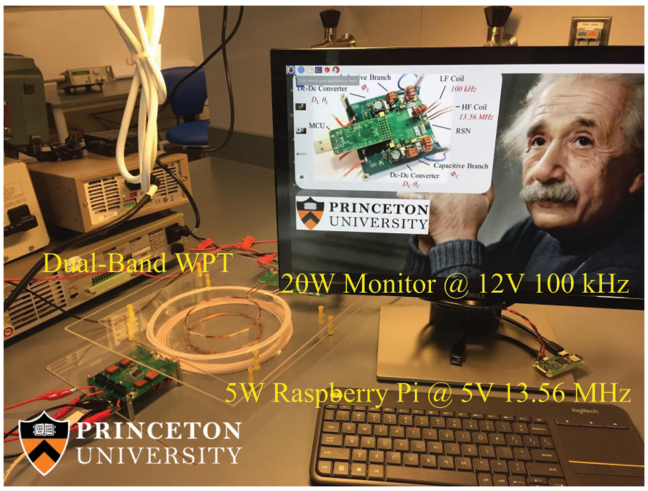

Fig. 1. Dual-band "complete" wireless desktop computer developed at Princeton Powerlab. The system simultaneously powers a 5-W Raspberry Pi at 13.56 MHz and a 20-W monitor at 100 kHz. The system is wirelessly powered and wirelessly connected to the Internet.

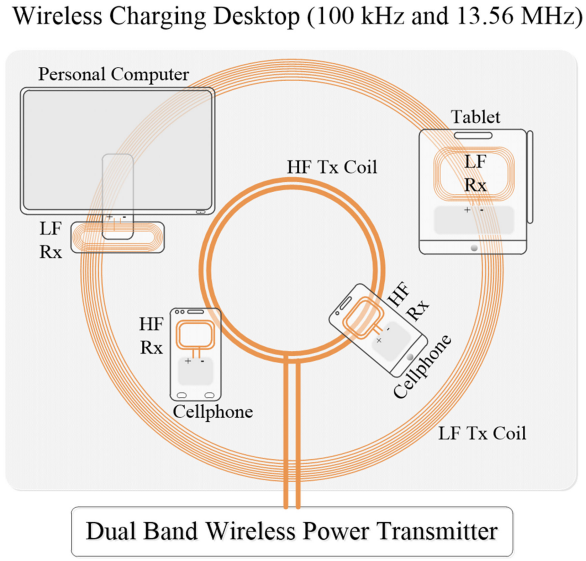

Fig. 2. Coil placement of a dual-band WPT desktop with multiple receivers operating at HF (13.56 MHz) and low frequency (LF) (100 kHz). The multiple receiving devices can be freely moved around and be continuously charged.

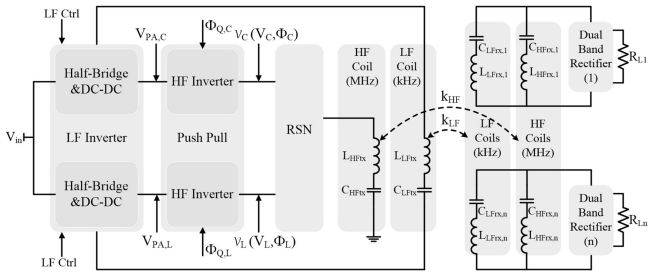

Fig. 3. Block diagram of a dual-band WPT system comprising an RSN-based dual-band transmitter and multiple reconfigurable dual-band receivers with different coupling coefficients.

functions as a synchronous half-bridge rectifier at 100 kHz, and functions as two series-stacked Class-E rectifiers at 13.56 MHz. Many components are reused at both frequencies. An online impedance estimation method was proposed to maintain ZVS of the high-frequency (HF) inverters. The prototype RSN transmitter can simultaneously deliver 30 W of power to multiple dual-band receivers (15 W maximum each) with 74.8% peak efficiency at 13.56 MHz with significant coil misalignment, and 82.5% peak efficiency at 100 kHz.

Fig. 1 shows a demo wireless desktop where a dual-band transmitter simultaneously powers a 5-W Raspberry Pi at 13.56 MHz and a 20-W monitor at 100 kHz. The Raspberry Pi interfaces with the monitor through HDMI. Other Internet of Things devices that support wireless charging may be added. The full demo desktop is completely wireless—it is wirelessly powered and wirelessly connected to the Internet. Fig. 2 shows the coil placement diagram. The transmitting coils and the receiving coils may be loosely coupled or closely coupled. The load impedance on the transmitter side may change across a wide range. The transmitter needs to maintain high performance at both kHz and MHz, and the receivers need to receive power from multiple frequencies with low component count.

The remainder of this paper is organized as follows. Section II provides an overview of the reconfigurable dual-band WPT system. The circuit topology and operation principles of the RSN and the RSN-based dual-band transmitter are presented in Section III. Section IV introduces the topology and operation principles of the reconfigurable dual-band receiver. Section V presents the prototype and experimental results, including detailed theoretical analysis and measured results of the dual-band transmitter and receiver. Finally, Section VI concludes this paper.

II. Overview of Dual-Band Multi-Receiver WPT

Fig. 3 shows the block diagram of the proposed dual-band WPT system including an RSN-based transmitter and multiple reconfigurable dual-band receivers. The RSN-based transmitter comprises two LF dc–dc converters operating at kHz (e.g., 100 kHz), one modified push–pull HF Class-E inverter operating at MHz (e.g., 13.56 MHz), an RSN, an LF transmitting coil, and an HF transmitting coil. The receiver side comprises multiple LF/HF receiving coils and multiple dual-band rectifiers. The two dc–dc converters modulate the two inputs of the modified push–pull Class-E inverter, and simultaneously drive the LF transmitting coil at 100 kHz. By modulating the voltage amplitude and the phase of the two HF inverters [29], the two inverter branches see pure resistive load. The dc–dc converters also drive the LF transmitting coil as a phase-shift full-bridge inverter, transferring power at LF to the receivers.

Each of the function blocks in the RSN-based transmitter can be implemented in multiple ways: the LF inverters can be implemented as Class-D or full-bridge inverters; the low-pass filters at the output of the LF inverters can be implemented as L-networks or π-networks; the push–pull inverters can be implemented as

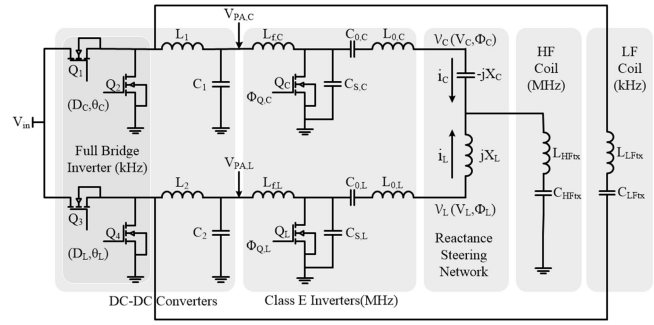

Fig. 4. Schematic of an example dual-band transmitter comprising an RSN, two HF Class-E inverters, two buck converters (with one half-bridge and one inductor), and two optimally tuned transmitting coils (one for each frequency).

Class-E, Class-F, or Class-Φ inverters; the RSN can be implemented as a three-port *LC* network or other three-port network options. The LF and HF transmitting and receiving coils are standard coils tuned for nominal coupling. The two half-bridge circuits drive the LF coil, and the two HF inverters drive the HF coil. The power delivered at the two frequencies can be modulated independently.

The receiver developed in this paper is a dual-band reconfigurable receiver (DBRR) that can operate at either 100 kHz or 13.56 MHz. The receiver functions as two series-stacked Class-E rectifier at 13.56 MHz, and functions as a half-bridge rectifier at 100 kHz. It has very low component count and can maintain high performance at both frequencies. A single dual-band receiver can be reprogrammed to function at either frequency, and multiple receivers working at different frequencies can be placed in adjacent to each other while all maintaining high performance. The transmitter sees the impedance of all receivers operating at two frequencies with their power added together. Finally, the RSN-based transmitter and the DBRR are merged together as a complete dual-band WPT system that operate at both frequencies. The transmitter can dynamically estimate the lumped load impedance and individually modulate the power delivered at each frequency.

III. Dual-Band RSN Transmitter With a Modified Push–Pull Class-E Inverter

Fig. 4 shows the schematic of an example implementation of the RSN-based dual-band transmitter. It comprises two half-bridge LF inverters, two *LC* low-pass filters, and two HF Class-E inverters. The two half-bridge inverters and the two low-pass filters function as two buck converters that modulate the inputs of the two Class-E inverters. The two Class-E inverters are loaded with an *LC* resonant network including an inductive branch jX_L and a capacitive branch $-jX_C$. The two Class-E inverters and the *LC* resonant network can be interpreted as a modified push–pull Class-E inverter. The two half-bridge inverters also drive an LF coil as a full-bridge inverter.

This RSN transmitter has the same component count as a traditional full-bridge inverter for LF operation and a push–pull Class-E inverter for HF operation. The key innovation of this design is to merge the LF and HF operation and maintain ZVS operation of the HF inverters against coil misalignment.

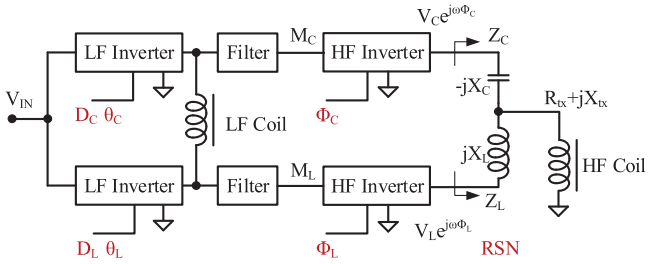

Fig. 5. Simplified block diagram of the RSN architecture. This architecture has six input variables: D_C, D_L, θ_C, θ_L, Φ_C, and Φ_L, and independently drives two coils at two frequencies.

A. Principles of the RSN

Fig. 5 shows a simplified block diagram of the dual-band transmitter with an RSN connected between the push–pull Class-E inverter and the HF coil. The RSN is a three-terminal network comprising an inductor and a capacitor. Derived from the RCN [14], [15], outphasing [16], and the ICN [18]–[20] concept, with modulated inverter dc inputs, the RSN splits the power flow to compensate the load impedance variation, so that the HF inverters can operate efficiently across a wide impedance range.

The RSN architecture has six control variables as follows: D_C and D_L are the duty ratios of the two LF inverters; θ_C and θ_L are the phases of the two dc–dc converters; and Φ_C and Φ_L are the phases of the two HF inverters. The two intermediate dc voltages M_C and M_L are controlled by D_C and D_L. To simplify the analysis, we assume $X_C = X_L = X_O$ and model the two HF inverters as two ac voltage sources—$V_C^* = V_C e^{j\Phi_C}$ and $V_L^* = V_L e^{j\Phi_L}$. X_O is the reactance of the inductive/capacitive branch. X_L and X_C are assumed to be equal to X_O. The amplitudes (V_L, V_C) and phases (Φ_L, Φ_C) can be independently modulated. Applying superposition rules, the effective load impedance of the two inverters Z_C and Z_L are explicit functions of X_O, R_{tx}, X_{tx}, and K_{LC}^*

$$Z_C = \frac{X_O^2}{R_{tx} - K_{LC}^* R_{tx} + (X_{tx} + X_O - K_{LC}^* X_{tx})j} \tag{1}$$

$$Z_L = \frac{X_O^2}{R_{tx} - \frac{1}{K_{LC}^*} R_{tx} + (X_{tx} - X_O - \frac{1}{K_{LC}^*} X_{tx})j}. \tag{2}$$

K_{LC}^* is the complex voltage ratio between the inductive branch and capacitive branch—$K_{LC}^* = \frac{V_L}{V_C} e^{j(\Phi_L - \Phi_C)}$. To ensure pure resistive Z_C and Z_L, we need

$$K_{LC} = \frac{V_L}{V_C} = \frac{X_{tx}\cos(\Delta_{LC}) - R_{tx}\sin(\Delta_{LC})}{X_{tx} - X_O} \tag{3}$$

$$\sin^2(\Phi_L - \Phi_C) = \sin^2\Delta_{LC} = \frac{X_O^2}{X_{tx}^2 + R_{tx}^2}. \tag{4}$$

Here, $\Delta_{LC} = \Phi_L - \Phi_C$ is the phase difference between the two HF inverters. For a load impedance range $R_{tx} \in [R_{\min}, R_{\max}]$, $X_{tx} \in [X_{\min}, X_{\max}]$, X_O should be selected such that $X_O^2 \le (X_{tx}^2 + R_{tx}^2)$ holds true across the entire R_{tx} and X_{tx} range, so that there is a solution for Δ_{LC}. For each pair

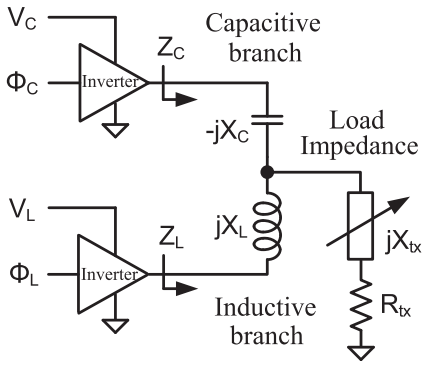

Fig. 6. Operation principles of the RSN. Amplitude and phase modulation of the HF inverters steer power between the two branches and perform reactance compensation. V_C, V_L, Φ_C, and Φ_L are the control variables.

of R_{tx} and X_{tx}, there are four feasible solutions for K_{LC}^*, one located in each quadrant. Due to phase and polarity symmetry, the solution in the first quadrant is equivalent to the solution in the third quadrant; and the solution for the second quadrant is equivalent to the solution in the fourth quadrant. Usually, the solution in the first (or third) quadrant is preferable because the range of K_{LC} in the first quadrant is smaller than the range of K_{LC} in the second (or fourth) quadrant. For example, according to (3) and (4), the range of K_{LC} in the first quadrant is from 0.707 to 1.414 and the range of K_{LC} in the 2nd is from 0.007 to 140.7, when R_{tx} =1 Ω, $X_O = 1j\Omega$, and X_{tx} varies from $-0.99j\Omega$ to $0.99j\Omega$. Thus, a first quadrant solution of K_{LC}^* is preferable because keeping Δ_{LC} close to zero can minimize the converter stress. The optimal solutions for K_{LC} and Δ_{LC} are as follows:

$$K_{LC} = |\frac{V_L}{V_C}| = |\frac{X_O + X_{tx}}{X_{tx}\cos(\Delta_{LC}) + R_{tx}\sin(\Delta_{LC})}| \quad (5)$$

$$\Delta_{LC} = \Phi_L - \Phi_C = \arcsin\sqrt{\frac{X_O^2}{X_{tx}^2 + R_{tx}^2}}. \quad (6)$$

For a typical voltage source inverter, V_L is linearly proportional to M_L and D_L, and V_C is linearly proportional to M_C and D_C. As a result, pure-resistive loading of the two HF inverters can be achieved by modulating D_C, D_L, Φ_C, and Φ_L. The control strategies for these variables are as follows.

1) If Z_{tx} is resistive, the two HF inverters equally share power and both see pure resistive load.
2) If Z_{tx} is inductive, the system steers power toward the capacitive branch. The capacitive element $-jX_C$ is used to compensate the inductive load Z_{tx}.
3) If Z_{tx} is capacitive, the system steers power toward the inductive branch. The inductive element jX_L is used to compensate the capacitive load Z_{tx}.

Fig. 6 illustrates the principles of the RSN. The amplitude and phase modulation of the two HF inverters (power amplifiers) steer power between the two branches of the RSN and dynamically compensate for the load reactance variation.

We quantitatively present the design of an example RSN system in detail as follows: assume R_{tx} varies from 1 to 5 Ω; X_{tx} varies from $-2j\Omega$ to $2j\Omega$; and X_O is selected as $1j\Omega$. Based on KCL and KVL, the effective resistances seen at the inductive branch (R_L) and capacitive branch (R_C) can be calculated based on (1) and (2), respectively. R_L and R_C can be used to estimate the power sharing between the two branches. Fig. 7(a)–(d) shows the K_{LC}, Δ_{LC}, R_L, and R_C as functions of R_{ts} and X_{ts}. As derived in [29], a voltage amplitude ratio adjustable from $1/\sqrt{2}$ to $\sqrt{2}$ and a phase shift adjustable from 0° to 90° can cover an arbitrary load impedance range.

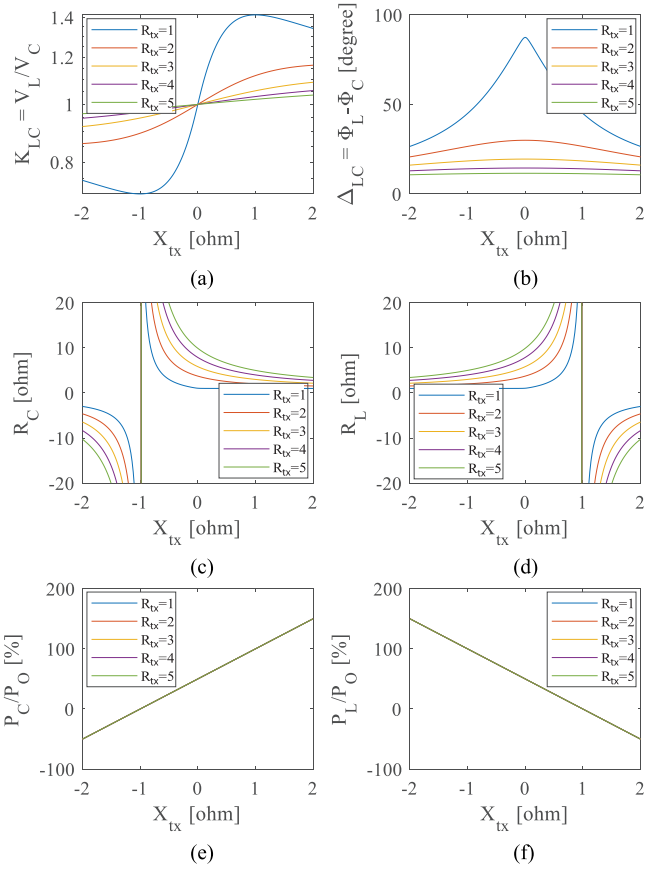

Fig. 7. Control variables as functions of the load reactance X_{tx}. (a) V_L/V_C. (b) Δ_{LC}. (c) Resistance of the capacitive branch. (d) Resistance of the inductive branch. (e) Percentage of the power on the capacitive branch. (f) Percentage of the power on inductive branch. P_C: Power of the capacitive branch; P_L: Power of the inductive branch; P_O: Output power.

As shown in Fig. 7, with an inductive load ($X_{tx} > 0$), V_L should be larger than V_C to deliver more power through the capacitive branch; with a capacitive load ($X_{tx} < 0$), V_L should be smaller than V_C to deliver more power through the inductive branch. When $|X_{tx}| \leq |X_O|$, both R_L and R_C are higher than the overall load resistance, indicating that the two inverters are sharing power. When $|X_{tx}| > |X_O|$ (i.e., the load reactance is very high), one of R_L and R_C is smaller than the overall load resistance, and the other one is negative, indicating that there exists circulating power between the two branches. In other words, when needed, one inverter branch functions as a rectifier to compensate the reactance variation.

Fig. 7(e) and 7(f) shows the percentage of the power sharing between the inductive and capacitive branches for this example

RSN design. As expected, with pure resistive loads (i.e., $X_{tx} = 0$), the two branches evenly share power (50% each branch); with capacitive loads ($X_{tx} < 0$), the inductive branch delivers more power than the capacitive branch; with inductive loads ($X_{tx} > 0$), the capacitive branch delivers more power than the inductive branch; with very high capacitive loads ($X_{tx} < -X_O$), power circulates from the inductive branch to the capacitive branch; and with very high inductive loads ($X_{tx} > X_O$), power circulates from the capacitive branch to the inductive branch.

The RSN can be implemented in many different ways. In general, the system steers power toward the inductive branch or capacitive branch to seamlessly compensate the reactance variation. Both the two HF inverters see pure resistive load. Compared to conventional designs, the proposed RSN architecture has the following advantages.

1) It can seamlessly compensate an arbitrary load impedance range and maintain pure resistive load.
2) It requires very few additional component compared to a push–pull Class-E inverter.
3) It has smooth transient behavior for load variation with no mode-switching spikes or harmonics.
4) The dc–dc converters in the RSN are reused to drive an LF transmitter.

B. Load Impedance Estimation and Control

Load impedance estimation allows WPT systems to operate at maximum power point and maintain high efficiency. Sophisticated ac voltage and/or current sensing circuitry are usually needed in existing HF designs. The unique configuration of the RSN architecture allows low-cost load impedance estimation for WPT without ac voltage/current sensors. The load impedance can be estimated with simple circuitry by comparing the dc power delivered by the two inverter branches. Based on (1) and (2), the input dc power of the two inverter branches, P_C and P_L, is calculated as follows:

$$P_C = \frac{V_C^2(R_{tx} - K_{LC}(R_{tx}\cos(\Delta_{LC}) - X_{tx}\sin(\Delta_{LC})))}{2X_O^2} \tag{7}$$

$$P_L = \frac{V_L^2(R_{tx} - \frac{1}{K_{LC}}(R_{tx}\cos(\Delta_{LC}) + X_{tx}\sin(\Delta_{LC})))}{2X_O^2}. \tag{8}$$

The ratio of the power delivered by the two branches is

$$\frac{P_L}{P_C} = K_{LC}^2 \frac{\eta_C(R_{tx} - \frac{1}{K_{LC}}(R_{tx}\cos(\Delta_{LC}) + X_{tx}\sin(\Delta_{LC})))}{\eta_L(R_{tx} - K_{LC}(R_{tx}\cos(\Delta_{LC}) - X_{tx}\sin(\Delta_{LC})))}. \tag{9}$$

Here, η_L and η_C are the efficiencies of the two dc–dc converters. Equation (9) indicates that the load impedances R_{tx} and X_{tx} are closely related to the input dc power ratio $\frac{P_L}{P_C}$ for a given η_L, η_C, K_{LC}, and Δ_{LC}. $\frac{P_L}{P_C}$ can be measured from the dc–dc converters with simple circuit and low cost.

Fig. 8 plots the relationship between the input dc power ratio P_L/P_C and load impedance $Z_{tx} = R_{tx} + jX_{tx}$ for $K_{LC} = 1$ and $\Delta_{LC} = 90°$. The load resistance can be estimated with the total input power $P_L + P_C$ and the voltage amplitudes.

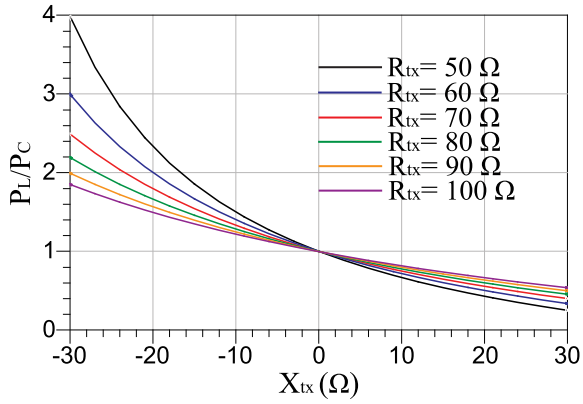

Fig. 8. Power ratio P_L/P_C as a function of the load impedance Z_{tx} for a specific K_{LC} value and Δ_{LC} value. This power ratio can be used to estimate the load impedance to enable maximum power point tracking and maximum efficiency tracking.

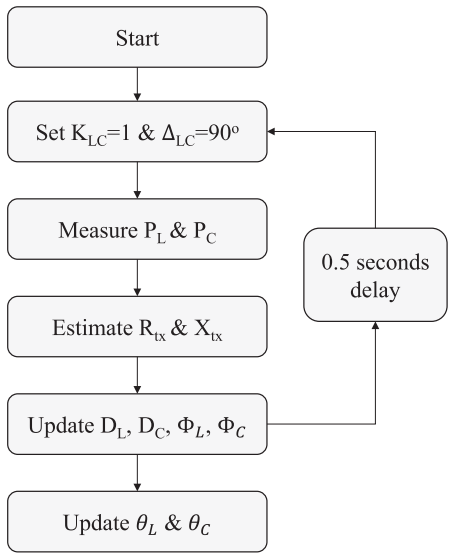

Fig. 9. Control flowchart of the impedance estimation. The impedance estimation process is repeated every 0.5 s.

Assume the efficiencies of the two inverters are the same, the load input impedance X_{tx} can be estimated with P_L/P_C using Fig. 8. Fig. 9 shows the control flowchart for the load impedance estimation. The input power of the *L* and *C* branches is sampled and the power ratio is calculated. Through a look-up table, the desired duty cycles (D_L and D_C) and the driving phases (ϕ_L and ϕ_C) can be obtained to control the dc–dc converters and Class-E inverters based on the calculated power ratio P_L and P_C.

C. LF Full-Bridge Transmitter

One way to implement the two dc–dc converters is to build them as two buck converters with two half-bridge inverters (see Fig. 5). The two half-bridge inverters can drive an LF coil as a phase-shifted full bridge, whereas at the same time modulate the dc voltages M_C and M_L for the HF inverters. The LF power

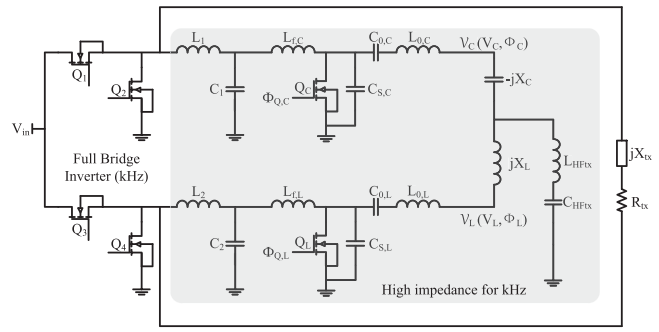

Fig. 10. Schematic of the dual-band transmitter with a phase-shifted full-bridge LF transmitter and an RSN-based HF transmitter. The two HF inverters look like two high impedance loads for the LF full-bridge inverter.

transfer is controlled by the phase of the two LF inverters θ_L and θ_C. The outputs M_L and M_C are controlled by D_L and D_C. Fig. 10 shows the schematic of the dual-band transmitter with the RSN-based HF transmitter shaded. Here, $R_{\mathrm{LF}tx}$ and $X_{\mathrm{LF}tx}$ are, respectively, the resistance and reactance of the LF coils. In this circuit, Q_1 and Q_2 operate as one phase-shifted half bridge, and Q_3 and Q_4 operate as the other phase-shifted half bridge. The duty ratios of the two half-bridges modulate M_C and M_L, and the phase difference between the two half-bridges modulates the power output of the LF transmitter.

Benefiting from the low-pass filters at the output of the dc–dc converters and the input inductors of the Class-E inverters, the power delivered by the LF transmitter and that delivered by the HF transmitter are well decoupled from each other. θ_C and θ_L modulate the LF transmitter, but have no impact on M_C and M_L, and thus have no impact on the power delivery of the HF transmitter. Similarly, Φ_C and Φ_L modulate the HF transmitter, but have no impact on the LF transmitter. When D_C and D_L are adjusted to modulate M_C and M_L, θ_C and θ_L should be changed accordingly to maintain the power levels of the LF transmitter. Similar to [4], the two overlapped transmitter coils and the related resonant tanks are optimally tuned for 100 kHz and 13.56 MHz, respectively.

IV. Dual-Band Reconfigurable Receiver

In many application scenarios, a wireless power receiver may need to be compatible with multiple standards. The receivers also need to be compact and efficient with low component count. A full-bridge synchronous rectifier can work at both HFs and LFs. However, the square-wave harmonic contents of the full-bridge rectifier raise concerns for many portable applications. It is also difficult to drive the high-side switches in a full-bridge rectifier. One can use Class-E rectifiers at HFs to reduce the harmonic contents, but the inductance of the choke inductor is usually large.

Fig. 11(a) shows the topology of a DBRR. The rectifier in the receiver comprises two switches Q_{r1} and Q_{r2}, two shunt capacitors C_{r1} and C_{r2}, two RF choke inductors, two filter capacitors, and one switch Q_s for mode selection. The dual-band rectifier can either work in the kHz range (e.g., 100 kHz), or work in the MHz range (e.g., 13.56 MHz), depending on if Q_s is OFF or ON. The parasitic capacitances of the diodes are absorbed into the shunt capacitors. Table I lists the component values of the proposed dual-band rectifier for 100-kHz and 13.56-MHz operation.

Fig. 11(b) and (c) illustrates the operation principles of the proposed rectifier in HF and LF, respectively. If Q_s is kept ON, the rectifier functions as two Class-E half-wave rectifiers stacked in series. The rectifier receives power from the HF coil (i.e., 13.56 MHz). If Q_s is kept OFF, the rectifier functions like a Class-D rectifier and receives power from the LF coil (i.e., 100 kHz). As shown in Fig. 11(c), the RF choke inductors (L_{f1} and L_{f2}) can be considered as short, and the shunt capacitors (C_{r1} and C_{r2}) can be considered as open. Q_s can be implemented as a low-speed switch in the controller IC. This inductor functions as a short circuit (with low impedance) at 100 kHz and a dc choke inductor (with high impedance) at 13.56 MHz.

Fig. 12(a) and (b) shows the simulated voltage waveforms of Q_{r1} and Q_{r2} working at 13.56 MHz and 100 kHz, respectively. At HFs, the rectifier functions as two Class-E rectifiers stacked in series and the waveform of the voltage across the switches is half-wave sinusoidal. At LFs, the rectifier functions as one Class-D rectifier and the voltage across the switches is rectangular. In 100-kHz operation, the shunt capacitors may resonate with the RF choke inductors, resulting in an HF ripple at $V_{Q_{r1}}$ and $V_{Q_{r2}}$. One can reduce the oscillation by using a small C_r at the cost of higher distortion at 13.56 MHz or using a small L_f at the cost of higher ac current across the inductors. Fig. 12(c) and (d) shows the simulated waveforms of the current and voltage of the mode selection switch at 13.56 MHz and 100 kHz, respectively. The blue lines are the dc output current and dc output voltage, respectively. The peak current flowing through Q_s is twice of the dc output current. The voltage across the mode selection switch is same as that of the switch Q_r, which can be used to choose the current and voltage rating of the switch Q_s.

Fig. 12(e) and (f) shows the simulated THD and the ratio of the switch peak voltage to the output voltage (the voltage stress of Q_{r_1} and Q_{r_2}), and the input impedance of the dual-band rectifier with different C_r values. The THD and the switch voltage stress can be reduced by increasing the C_r. However, a larger C_r will reduce the input resistance of the rectifier, which may increase the conduction loss in the receiving coil, the RF choke inductor, and the rectifier switches.

The design principles of the dual-band rectifier are as follows.

1) The shunt capacitor C_r should be designed on the THD requirement, voltage stress, and the ac self-resistance of the receiving coil.
2) The mode selection switch Q_s should be implemented as a low-speed switch with low ON-resistance. Its voltage rating is the same as the two high speed switches Q_{r_1} and Q_{r_2}.
3) The inductors should be designed so that they function as RF choke inductors at HFs and function as shorts at LFs.
4) The output filter capacitor C_f should be big enough to eliminate the output voltage ripple.

At HFs (e.g., 13.56 MHz), the optimal duty ratio of the switches in the dual-band rectifier depends on the load impedance. Fig. 13(a) and (b) shows the optimal duty ratio and

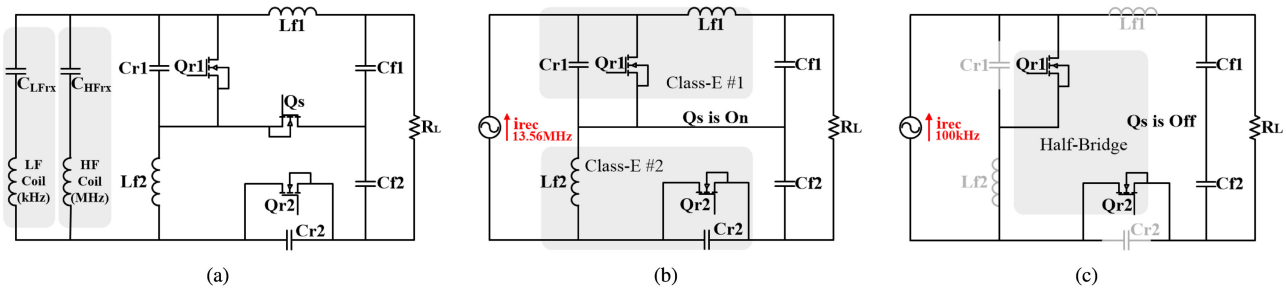

Fig. 11. Topology of the dual-band receiver. (a) Schematic of the dual-band receiver. (b) Schematic of the rectifier when it operates at HF with Q_S ON. (c) Schematic of the rectifier when it operates at LF with Q_S OFF.

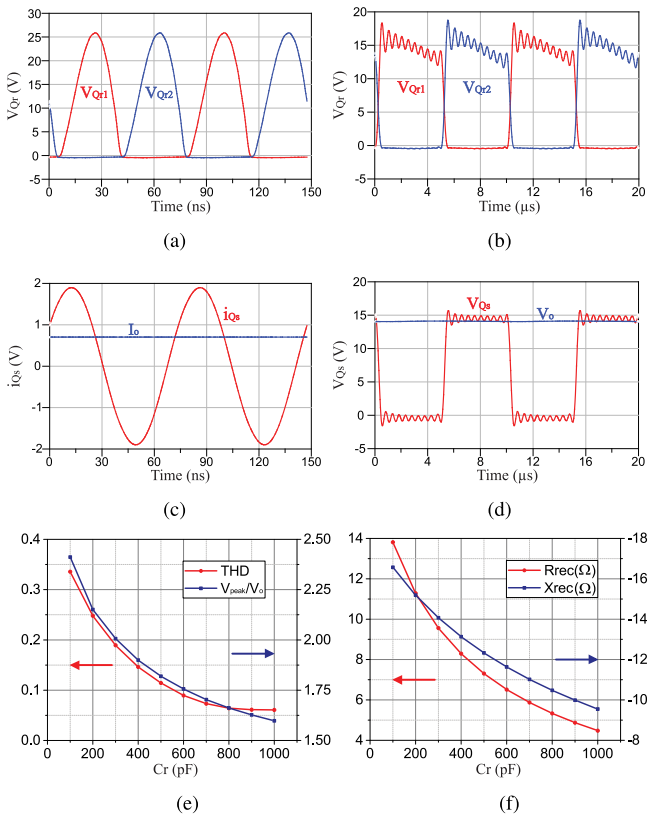

Fig. 12. (a) Simulated drain-to-source voltage of Q_r at 13.56 MHz. (b) Simulated drain-to-source voltage of Q_r at 100 kHz. (c) Simulated current waveform of the mode selection switch Q_s at 13.56 MHz. (d) Simulated voltage waveform of the mode selection switch Q_s at 100 kHz. (e) Simulation THD and the ratio of the switch peak voltage to the output voltage (voltage stress of the switch). (f) Simulated rectifier input impedance.

TABLE I
PARAMETERS OF THE EXAMPLE DUAL-BAND RECTIFIER

L_{f1}	C_{r1}	L_{f2}	C_{r2}	C_{f1}	C_{f2}
1.2 μH	500 pF	1.2 μH	500 pF	20 μF	20 μF

voltage stress of the switches for a range of R_L. The optimal duty ratio decreases as R_L increases. Since the dual-band rectifier functions as two series-stacked Class-E half-wave current-driven rectifier, the voltage stress of each HF switch is only one half of the voltage stress of a conventional Class-E current-driven

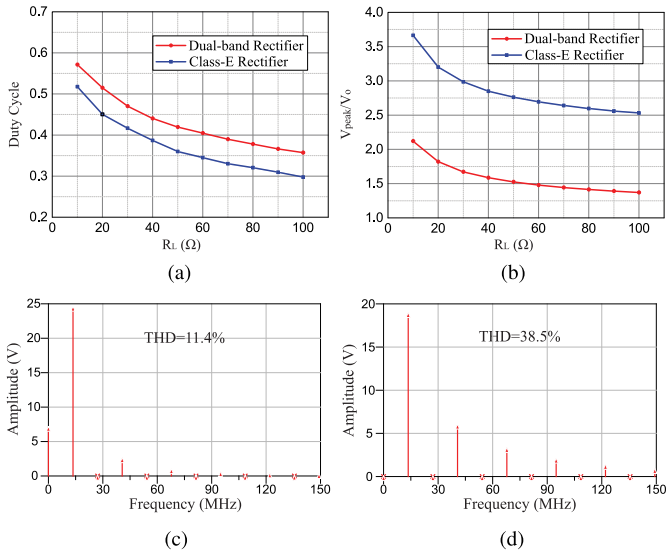

Fig. 13. (a) Simulated optimal rectifier duty cycle at 13.56 MHz. (b) Simulated switch voltage stress at 13.56 MHz. (c) Simulated THD of the dual-band rectifier at 13.56 MHz. (d) Simulated THD of the full-bridge rectifier at 13.56 MHz.

rectifier [30]. For LF operation, the voltage stress of the two switches is identical to that of a half-bridge rectifier. Fig. 13(c) and (d) shows the simulated THD of the dual-band rectifier and the full-bridge rectifier operating at 13.56 MHz. As expected, the dual-band reconfigurable rectifier works as two series-connected Class-E rectifiers and offers significantly lower THD than a full-bridge rectifier.

Compared to a system with two separate rectifiers designed for one frequency each, the proposed dual-band rectifier offers the following advantages.

1) High efficiency at both kHz and MHz operation.
2) Lower voltage stress than a Class-E rectifier, and lower harmonic distortion than a full-bridge rectifier.
3) Very low component count (the dual-band rectifier only has one additional low speed switch Q_s than a Class-E full-wave rectifier or a half-bridge rectifier).
4) Simple sensing, control, and gate drive circuitry. The HF and LF sensing and control circuitry, as well as the mode-selection switch, can be integrated in a single chip.

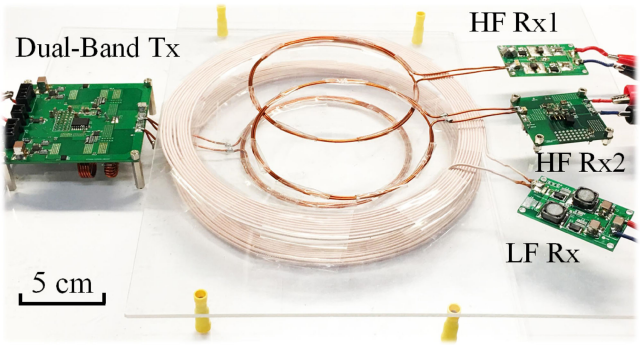

Fig. 14. Prototype dual-band WPT system with a RSN-based transmitter, a pair of HF coils, a pair of LF coils, and one active HF receiver, one passive HF receiver, and one passive LF receiver.

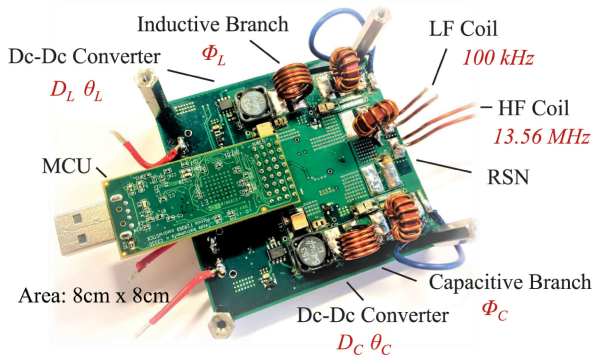

Fig. 16. Dual-band transmitter with two dc–dc converters, a push–pull Class-E inverter, a RSN, and a microcontroller (TI F28069). Power is jointly delivered by the inductive branch and the capacitive branch.

TABLE II
PARAMETERS OF THE COUPLING COILS

$L_{tx,LF}$ 36 μH	$r_{tx,LF}$ 0.2 Ω	$C_{tx,LF}$ 70 nF	$L_{rx,LF}$ 36 μH	$r_{rx,LF}$ 0.2 Ω	$C_{rx,HF}$ 80 nF
$L_{tx,HF}$ 3.5 μH	$r_{tx,HF}$ 2 Ω	$C_{tx,HF}$ 40 pF	$L_{rx,HF}$ 1.2 μH	$r_{rx,HF}$ 0.5 Ω	$C_{rx,HF}$ 130 pF

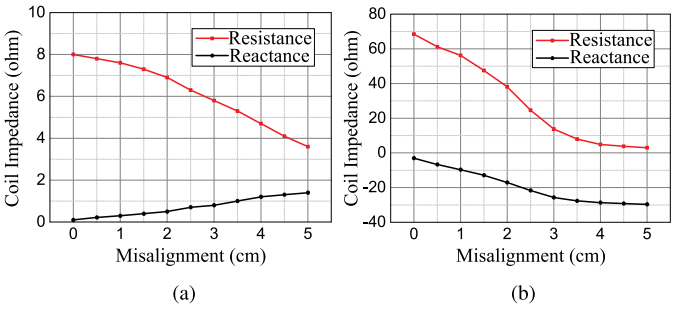

Fig. 15. Measured input impedances of the LF and HF coils against coil misalignment. (a) Input impedance of the LF coil. (b) Input impedance of the HF coil.

TABLE III
PASSIVE COMPONENT VALUES OF THE DUAL-BAND TRANSMITTER

$L_{f,C}$ 200 nH	$L_{0,C}$ 1650 nH	$C_{S,C}$ 260 pF	$C_{0,C}$ 83 pF	C_{RSN} 397 pF	C_1 20 uF	L_1 10 uH
$L_{f,L}$ 200 nH	$L_{0,L}$ 1650 nH	$C_{S,L}$ 260 pF	$C_{0,L}$ 83 pF	L_{RSN} 350 nH	C_2 20 uF	L_2 10 uH

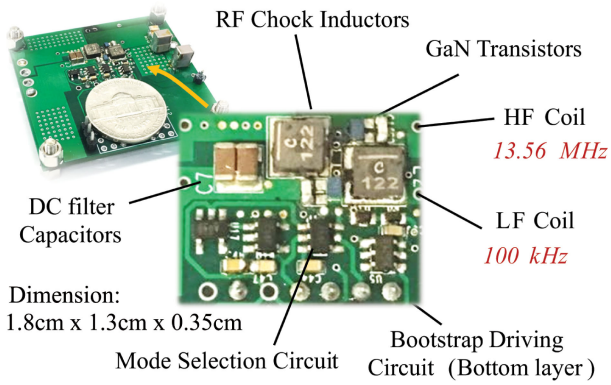

Fig. 17. Active dual-band rectifier with two GaN transistors, the mode selection and bootstrap driving circuits. The power density is 300 W/in^3.

In summary, the proposed dual-band rectifier is a promising option for future practical designs where high performance and low component count are needed. The key principles of this rectifier are to merge high efficiency LF rectifiers (e.g., Class-D) with low distortion HF rectifiers (e.g., Class-E), without increasing the component count and the device stress. When designing this rectifier, the LF rectifier and HF rectifier should be jointly optimized so that they share the same loss budget when delivering the same amount of power with the same thermal limit.

V. EXPERIMENTAL VERIFICATION

Fig. 14 shows a prototype dual-band WPT system comprising a 100-kHz transmitter, a 13.56-MHz transmitter, a 100-kHz receiver, and two 13.56-MHz receivers (one passive and one active). The operating frequency, 13.56 MHz from the ISM band, is chosen to demonstrate the effectiveness of the proposed architecture with a more compact prototype, and to explore the limitations of the proposed architecture. Measured parameters of the coupling coils are listed in Table II. Fig. 15 shows the measured input impedances of the LF and HF coils under a varying misalignment. Here, the impedance variation is jointly determined by the mutual and self-inductance, cross coupling, compensation capacitance, and load impedance of the LF and HF coils. The impedance of the HF coil highly depends on the coil misalignment. Fig. 16 shows a picture of the dual-band transmitter. Key parameters of the dual-band transmitter are listed in Table III. $L_{f,C}$ and $L_{f,L}$ are designed to resonate with $C_{S,C}$ and $C_{S,L}$ following the method described in [17]. The resonant frequency of the output tank of the two Class-E inverters, $L_{0,C}$ and $C_{0,C}$, $L_{0,L}$ and $C_{0,L}$, is 13.56 MHz. The two HF switches are implemented as GaN transistors (GS66504B). The output capacitances of the two HF switches are absorbed into $C_{S,C}$ and $C_{S,L}$. Fig. 17 shows a picture of the dual-band reconfigurable rectifier.

A 100-kHz receiver and a 13.56-MHz receiver are designed and tested to evaluate the performance of the dual-band WPT

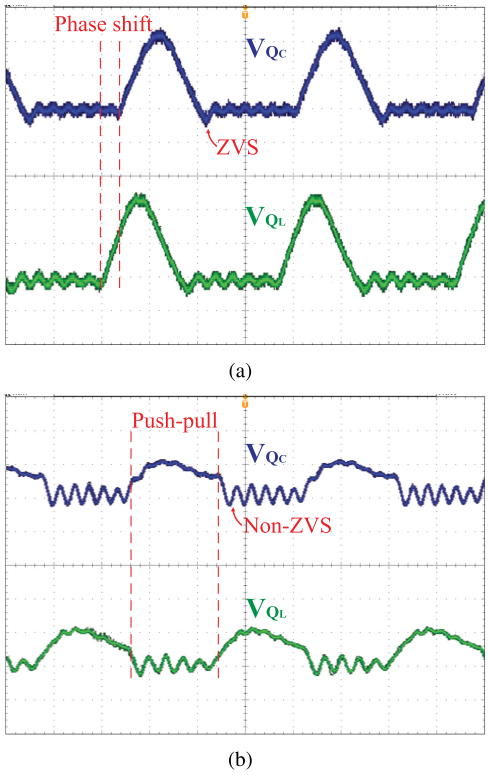

Fig. 18. Measured drain-to-source voltage waveforms of the two HF switches (30 V/div, 20 ns/div). (a) Switches achieve ZVS with RSN and phase shift. (b) Switches lost ZVS without RSN and phase shift (operate as a traditional push–pull Class-E inverter).

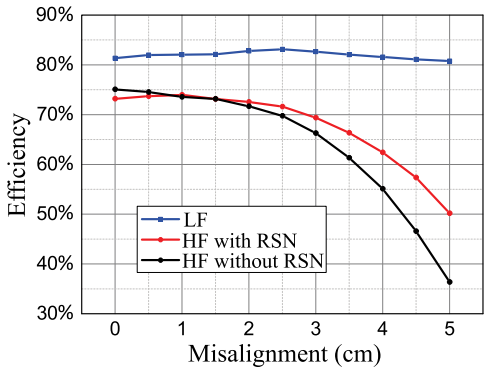

Fig. 19. Measured end-to-end efficiency of the dual-band WPT system. The radius of the HF coil is 5 cm, and the radius of the LF coil is 10 cm. The RSN significantly improved the system efficiency when the coil misalignment is large.

system. The dual-band reconfigurable rectifier (see Fig. 17) is used as the 100-kHz receiver when Q_s is OFF and as the 13.56-MHz receiver when Q_s is ON, respectively. The diameters of the HF coil and the LF coil are 10 and 20 cm, respectively. The distance between the transmitting coil and the receiving coils is 2.8 cm. The maximum horizontal misalignment is 5 cm. Fig. 18 shows the ZVS operation of the HF switches with Z_{tx} ($= 14 - j26\ \Omega$). The system delivers 10 W with and without RSN at 13.56 MHz. The RSN enables ZVS of both switches with appropriate phase and amplitude modulation. Fig. 19 shows the measured end-to-end efficiency of the 100-kHz WPT system

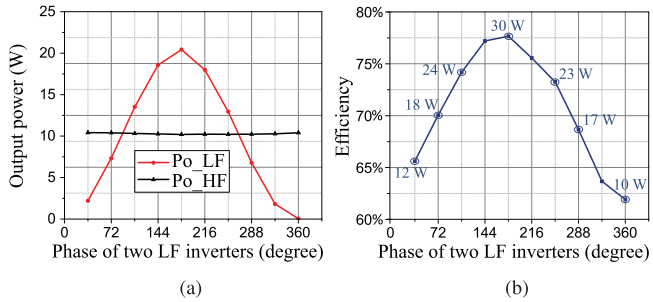

Fig. 20. Measured power and overall efficiency of the dual-band WPT system (HF and LF systems together). The system can maintain the power delivered at the HF (Po_HF) and modulate the power delivered at the LF (Po_LF). This is achieved by modulating the phase shift of the two LF inverters (θ_L and θ_C).

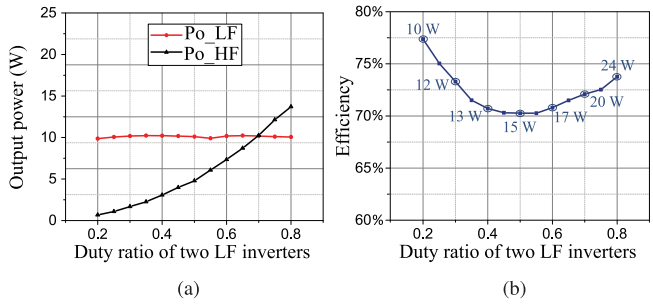

Fig. 21. Measured power and overall efficiency of the dual-band WPT system (HF and LF systems together). The system can maintain the power delivered at the LF (Po_LF) and modulate the power delivered at the HF (Po_HF). This is achieved by modulating the duty ratios of the two LF inverters (D_L and D_C).

and the 13.56-MHz WPT system with and without using the RSN. As shown in Fig. 19, the system with the RSN achieves higher efficiency than the system without the RSN across the entire misalignment range. Up to 13% of efficiency improvements are observed with significant load reactance (e.g., with 5 cm misalignment). We also observed that the presence of LF coil reduces the quality factor of the HF coil, and thus reduces the system efficiency with large coil misalignments. The efficiency of the dual-band WPT system can be improved by increasing the Q of the dual-band coils (through better materials and better two-dimensional layout).

Figs. 20 and 21 show the measured power and efficiency of the LF and HF systems working together. The system can independently modulate the power delivered by the LF and HF coils. The power delivered by the LF coil is controlled by the duty ratios D_L and D_C, and the phase shifts θ_L and θ_C. The power delivered by the HF coil is controlled by the intermediate voltages M_L and M_C, and the phases Φ_L and Φ_C. The operation of the two frequency bands is independent from each other with negligible cross-coupling effects. As shown in Fig. 20, by keeping D_L, D_C, Φ_L, and Φ_C as constants, and modulating the phase difference between θ_L and θ_C from 0 to 2π, the power transferred at 100 kHz (Po_LF) can be modulated between 0 and 20 W, and the power transferred at 13.56 MHz (Po_HF) can be kept constant at 10 W. Similarly, as shown in Fig. 21, one can keep the power transferred at 100 kHz constant at 10 W, and

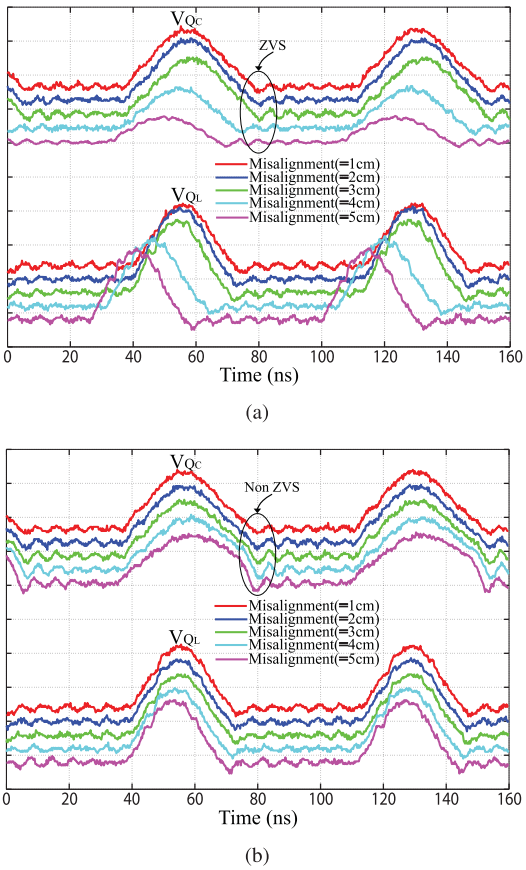

Fig. 22. Measured drain-to-source voltage waveforms of the Class-E inverters with the coil misalignment changing from 1 to 5 cm. (a) With phase shift and ZVS (50 V/div). (b) Without phase shift and non-ZVS (50 V/div).

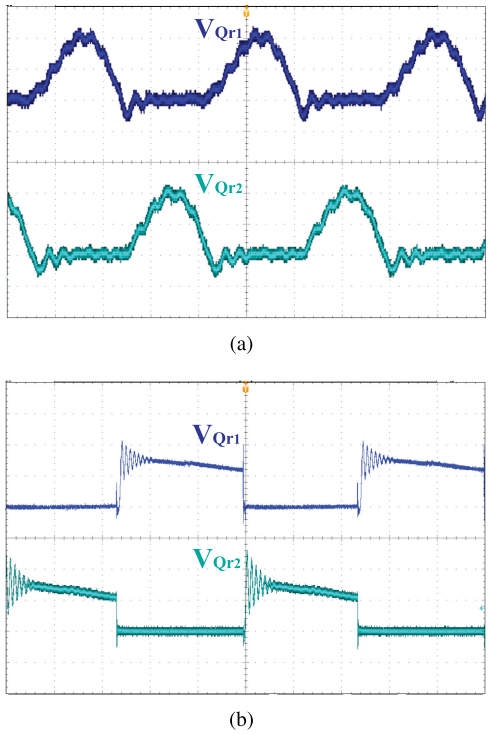

Fig. 23. Measured waveforms of the active dual-band rectifier. (a) Drain-to-source voltage at 13.56 MHz (10 V/div, 20 ns/div). (b) Drain-to-source voltage at 100 kHz (10 V/div, 2 μs/div).

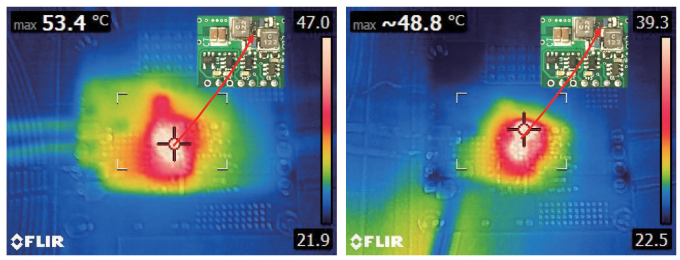

(a) (b)

Fig. 24. Thermal images of the active dual-band rectifier with the output power of 15 W. (a) 13.56-MHz operation. (b) 100-kHz operation.

modulates the power transferred at 13.56 MHz from 0 to 15 W by changing the duty ratio of the LF inverters. The measured efficiencies of the HF and LF transmitters working together are also shown in Figs. 20 and 21. When delivering 10 W of power at 13.56 MHz, and delivering 20 W of power at 100 kHz, the system reaches a maximum end-to-end efficiency of 77.7%.

Fig. 22 shows the measured drain-to-source voltage waveforms of the Class-E inverters with and without the RSN. The coil misalignment changes from 1 to 5 cm. The Class-E inverters operate in ZVS across the entire coil misalignment range with the RSN. D_L/D_C and Δ_{LC} are automatically selected from a look-up table according to the measured dc power ratio P_L/P_C (following Fig. 9).

The rectifiers reported in the previous measurement results were implemented with passive diodes. To further improve the system end-to-end efficiency, a dual-band rectifier implemented with synchronous GaN transistors is built and tested (see Fig. 11). The dimension of the active rectifier is 1.8 cm $\times$ 1.3 cm. The driving and auxiliary circuitries are all included. Based on the analysis in Section IV, the shunt capacitors of the dual-band rectifier C_{r1} and C_{r2} are 500 pF and the ratio $V_{\rm peak}/V_o$ is about 1.82 (see Fig. 12). The maximum dc output voltage of Q_{r1} and Q_{r2} (V_{DS}=40 V) is about 22 V and the maximum output power is 15 W at 13.56 MHz. A low-cost and low ON-resistance MOSFET ECH8420 is used as the mode selection switch Q_s. The RF choke inductors L_{r1} and L_{r2} are chosen as 1.2 μH, which behave as high impedance (about 102 $j\Omega$) at 13.56 MHz to block the HF current (reduce the ac power loss). They behave as short at 100 kHz. Fig. 23 shows the measured waveforms of the dual-band rectifier when working at HF and LF, respectively. The measured waveforms closely match with simulations (see Fig. 12). Fig. 24 shows the thermal images of the active dual-band rectifier when receiving 15 W.

Fig. 25(a) compares the measured dc–dc efficiency of the WPT system at 13.56 MHz with and without synchronous rectification. Fig. 25(b) does the same comparison for 100-kHz operation. As expected, synchronous rectification significantly improves the system efficiency across the full power range. Table IV lists a comprehensive comparison among this paper and

TABLE IV
COMPARISON AGAINST OTHER DUAL-BAND WPT DESIGNS

	Frequency	Power (W)	Efficiency	Misalignment	Control	Other Technologies
[7]	6.78 MHz/100-200 kHz	5/5	66%/72%	n/a	n/a	n/a
[8]	6.78 MHz/100-315 kHz	5/5	65%/65%	n/a	n/a	n/a
[9]	13.56 MHz/110 kHz	n/a	n/a	10 mm	n/a	n/a
[10]	6.78 MHz/200 kHz	9/7.4	78%/70.6%	n/a	n/a	n/a
[11]	6.78 MHz/87-300 kHz	10/10	65%/65%	n/a	MFPWM	n/a
[12]	6.78 MHz/200 kHz	n/a	74%/55% (coil)	20 mm	n/a	n/a
[29]	13.56 MHz/100 kHz	10/10	72.5%/81%	30 mm	n/a	RSN
This work	13.56 MHz/100 kHz	15/15	74.8%/82.5%	50 mm	Look-up Table	RSN and DBRR

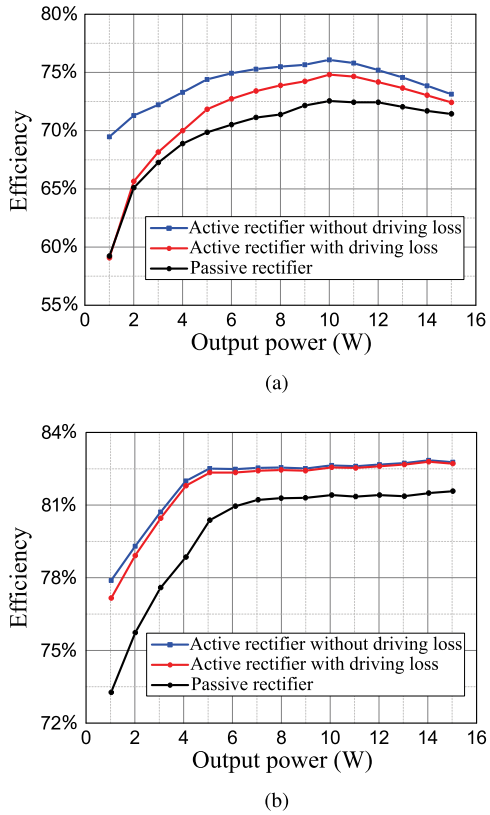

Fig. 25. Measured efficiency of the dual-band reconfigurable rectifiers. (a) 13.56-MHz operation. (b) 100-kHz operation.

existing works. This paper has the following four key contributions:

1) the RSN that can maintain the ZVS operation for the HF inverters across a wide load impedance range;
2) a GaN-based dual-band reconfigurable rectifier;
3) a load impedance estimation and control method;
4) a full demonstration of the dual-band WPT architecture and topology with shared switches and lower component count than conventional solutions.

VI. CONCLUSION

A dual-band multi-receiver WPT architecture targeting large coil misalignment and significant impedance variation is presented in this paper. This architecture is developed based on a novel RSN that can precisely compensate an arbitrary load reactance by dynamically steering the power between two inverter branches. We developed the theory of RSN and presented a design method that can cover a wide reactance variation range. To justify the additional component needed by the RSN, this paper also presents the topology and operation principles of a dual-band reconfigurable rectifier that can achieve high performance at both 100 kHz and 13.56 MHz. The dual-band inverter and dual-band receiver function together as a complete dual-band WPT system with high performance. The effectiveness of the proposed architecture is verified by a 30-W dual-band WPT prototype that can efficiently and independently power multiple 100-kHz and 13.56-MHz receivers with significant coil misalignment and load variation. The RSN architecture and the DBRR are applicable to a wide range of WPT enabled applications.

REFERENCES

[1] S. Y. R. Hui, W. Zhong, and C. K. Lee, "A critical review of recent progress in mid-range wireless power transfer," *IEEE Trans. Power Electron.*, vol. 29, no. 9, pp. 4500–4511, Sep. 2014.
[2] A. P. Hu, *Wireless/Contactless Power Supply: Inductively Coupled Resonant Converter Solutions*. Saarbrucken, Germany: VDM Publ., 2009.
[3] G. Buja, M. Bertoluzzo, and K. N. Mude, "Design and experimentation of WPT charger for electric city car," *IEEE Trans. Ind. Electron.*, vol. 62, no. 12, pp. 7436–7447, Dec. 2015.
[4] B. H. Choi, V. X. Thai, E. S. Lee, J. H. Kim, and C. T. Rim, "Dipole-coil-based wide-range inductive power transfer systems for wireless sensors," *IEEE Trans. Ind. Electron.*, vol. 63, no. 5, pp. 3158–3167, May 2016.
[5] T. Campi, S. Cruciani, F. Palandrani, V. De Santis, A. Hirata, and M. Feliziani, "Wireless power transfer charging system for AIMDs and pacemakers," *IEEE Trans. Microw. Theory Techn.*, vol. 64, no. 2, pp. 633–642, Feb. 2016.
[6] S. Li, W. Li, J. Deng, T. D. Nguyen, and C. C. Mi, "A double-sided LCC compensation network and its tuning method for wireless power transfer," *IEEE Trans. Veh. Technol.*, vol. 64, no. 6, pp. C2261–C2273, Jun. 2015.
[7] P. S. Riehl *et al.*, "Wireless power systems for mobile devices supporting inductive and resonant operating modes," *IEEE Trans. Microw. Theory Techn.*, vol. 63, no. 3, pp. 780–790, Mar. 2015.
[8] M. de Rooij and Y. Zhang, "A 10 W multi-mode capable wireless power amplifier for mobile devices," in *Proc. PCIM Asia; Int. Exhib. Conf. Power Electron., Intell. Motion, Renewable Energy Energy Manage.*, Shanghai, China, 2016, pp. 1–8.
[9] T. Sekiguchi, H. Odanaka, Y. Okano, and S. Ogino, "Study on the effective loading method of the magnetic sheet for NFC/WPT dual-band antenna," in *Proc. Int. Symp. Antennas Propag.*, Okinawa, Japan, 2016, pp. 946–947.
[10] D. Ahn and P. P. Mercier, "Wireless power transfer with concurrent 200-kHz and 6.78-MHz operation in a single-transmitter device," *IEEE Trans. Power Electron.*, vol. 31, no. 7, pp. 5018–5029, Jul. 2016.
[11] C. Zhao and D. Costinett, "GaN-based dual-mode wireless power transfer using multifrequency programmed pulse width modulation," *IEEE Trans. Power Electron.*, vol. 64, no. 11, pp. 9165–9176, Nov. 2017.
[12] M. Kung and K. Lin, "Dual-band coil module with repeaters for diverse wireless power transfer applications," *IEEE Trans. Microw. Theory Techn.*, vol. 66, no. 1, pp. 332–345, Jan. 2018.

[13] N. O. Sokal and A. D. Sokal, "Class E-A new class of high-efficiency tuned single-ended switching power amplifiers," *IEEE J. Solid-State Circuits*, vol. SSC-10, no. 3, pp. 168–176, Jun. 1975.
[14] Y. Han, O. Leitermann, D. A. Jackson, J. M. Rivas, and D. J. Perreault, "Resistance compression networks for radio-frequency power conversion," *IEEE Trans. Power Electron.*, vol. 22, no. 1, pp. 41–53, Jan. 2007.
[15] J. Choi, J. Xu, R. Makhoul, and J. M. Rivas Davila, "Implementing an impedance compression network to compensate for misalignments in a wireless power transfer system," *IEEE Trans. Power Electron.*, vol. 34, no. 5, pp. 4173–4184, May 2019.
[16] D. J. Perreault, "A new power combining and outphasing modulation system for high-efficiency power amplification," *IEEE Trans. Circuits Syst. I, Reg. Papers*, vol. 58, no. 8, pp. 1713–1726, Aug. 2011.
[17] L. Roslaniec, A. S. Jurkov, A. A. Bastami, and D. J. Perreault, "Design of single-switch inverters for variable resistance/load modulation operation," *IEEE Trans. Power Electron.*, vol. 30, no. 6, pp. 3200–3214, Jun. 2015.
[18] J. Lu, D. J. Perreault, D. M. Otten, and K. Afridi, "Impedance control network resonant DC-DC converter for wide-range high-efficiency operation," *IEEE Trans. Power Electron.*, vol. 31, no. 7, pp. 5040–5056, Jul. 2016.
[19] S. J. Gunter, K. K. Afridi, D. M. Otten, R. A. Abramson, and D. J. Perreault, "Impedance control network resonant step-down DC-DC converter architecture," in *Proc. IEEE Energy Convers. Congr. Expo.*, Montreal, QC, Canada, 2015, pp. 539–547.
[20] W. Inam, K. K. Afridi, and D. J. Perreault, "High efficiency resonant DC/DC converter utilizing a resistance compression network," *IEEE Trans. Power Electronic.*, vol. 29, no. 8, pp. 4126–4135, Aug. 2014.
[21] A. Kumar, S. Sinha, A. Sepahvand, and K. Afridi, "Improved design optimization for high-efficiency matching networks," *IEEE Trans. Power Electron.*, vol. 33, no. 1, pp. 37–50, Jan. 2018.
[22] S. Liu, M. Liu, S. Han, X. Zhu, and C. Ma, "Tunable class E^2 dc-dc converter with high efficiency and stable output power for 6.78 MHz wireless power transfer," *IEEE Trans. Power Electron.*, vol. 33, no. 8, pp. 6877–6886, Aug. 2018.
[23] S. Sinha, A. Kumar, and K. K. Afridi, "Active variable reactance rectifier: A new approach to compensating for coupling variations in wireless power transfer systems," in *Proc. IEEE Workshop Control Model. Power Electron.*, Stanford, CA, USA, 2017, pp. 1–8.
[24] S. Cochran, F. Quaiyum, A. Fathy, D. Costinett, and S. Yang, "A GaN-based synchronous rectifier for WPT receivers with reduced THD," in *Proc. IEEE PELS Workshop Emerg. Technol., Wireless Power Transfer*, Knoxville, TN, USA, 2016, pp. 81–87.
[25] M. Chen, "Merged multi-stage power conversion: A hybrid switched capacitor/magnetics approach," Ph.D. dissertation, Elect. Eng. Comput. Sci. Dept., Massachusetts Inst. Technol., Cambridge, MA, USA, 2015.
[26] M. Chen, K. K. Afridi, S. Chakraborty, and D. J. Perreault, "Multitrack power conversion architecture," *IEEE Trans. Power Electron.*, vol. 32, no. 1, pp. 325–340, Jan. 2017.
[27] M. Chen, S. Chakraborty, and D. J. Perreault, "Multitrack power factor correction architecture," *IEEE Trans. Power Electron.*, vol. 34, no. 3, pp. 2454–2466, Mar. 2019.
[28] H. Kim, H. Chen, D. Maksimovic, and R. Erickson, "Design of a high efficiency 30 kW boost composite converter," in *Proc. IEEE Energy Convers. Congr. Expo.*, Sep. 20–24, 2015, pp. 4243–4250.
[29] M. Liu and M. Chen, "Dual-band multi-receiver wireless power transfer with reactance steering network," in *Proc. IEEE PELS Workshop Emerg. Technol., Wireless Power Transfer*, Montreal, QC, Canada, 2018, pp. 1–6.
[30] J. A. Santiago-González, K. M. Elbaggari, K. K. Afridi, and D. J. Perreault, "Design of class E resonant rectifiers and diode evaluation for VHF power conversion," *IEEE Trans. Power Electron.*, vol. 30, no. 9, pp. 4960–4972, Sep. 2015.

Ming Liu (S'15–M'17) received the B.S. degree from Sichuan University, Chengdu, China, in 2007, and the Ph.D. degree in electrical and computer engineering from the University of Michigan-Shanghai Jiao Tong University Joint Institute, Shanghai Jiao Tong University, Shanghai, China, in 2017.

He is currently a Postdoctoral Research Fellow with the Department of Electrical Engineering, Princeton University, Princeton, NJ, USA. His research interests include circuit topology and architecture, control strategy, optimization-based design methods for megahertz wireless power transfer, and high-frequency power electronics.

Dr. Liu was the recipient of the Top-10 Academic Star Award and Excellent Ph.D. Thesis Award Nomination at Shanghai Jiao Tong University, and the Research Excellence Award from AirFuel Alliance.

Minjie Chen (S'10–M'15) received the B.S. degree from Tsinghua University, Beijing, China, in 2009, and the S.M., E.E., and Ph.D. degrees from the Massachusetts Institute of Technology (MIT), Cambridge, MA, USA, in 2012, 2014, and 2015, respectively.

In 2016, he was a Postdoctoral Research Associate with the MIT. In 2017, he joined, as an Assistant Professor, the Department of Electrical Engineering and Andlinger Center for Energy and the Environment, Princeton University, Princeton, NJ, USA, where he leads the Princeton Power Electronics Research Lab. His research interests include high-frequency power electronics, advanced power electronics architectures, power magnetics, and the design of high-performance power electronics for emerging and important applications.

Dr. Chen was the recipient of the NSF CAREER Award, the Outstanding Ph.D. Thesis Award from the Chorafas Foundation and MIT, two Transactions Prize Paper awards from theIEEE TRANSACTIONS ON POWER ELECTRONICS, the Siebel Energy Institute Seed Grant, an IEEE ECCE Best Demonstration Award, and a First Place Award from the Innovation Forum of Princeton University. He is an Associate Editor for the IEEE TRANSACTIONS ON POWER ELECTRONICS, a Guest Associate Editor for the IEEE JOURNAL OF EMERGING AND SELECTED TOPICS IN POWER ELECTRONICS, and an Associate Technical Program Committee Chair of the IEEE Energy Conversion Congress and Exposition.